Journal of Molecular Cell Biology (2023), 15(8), mjad050 https://doi.org/10.1093/jmcb/mjad050
Published online August 11, 2023

Article

CAMSAP2 and CAMSAP3 localize at microtubule intersections to regulate the spatial distribution of microtubules

Rui Zhang[1,†], Lusheng Gu[2,3,4,†], Wei Chen[5,†], Nobutoshi Tanaka[6], Zhengrong Zhou[1], Honglin Xu[1], Tao Xu[2,3,4], Wei Ji[2,3,4,*], Xin Liang[5,*], and Wenxiang Meng[1,2,7,*]

[1] State Key Laboratory of Molecular Developmental Biology, Institute of Genetics and Developmental Biology, Chinese Academy of Sciences, Beijing 100101, China
[2] College of Advanced Agricultural Sciences, University of Chinese Academy of Sciences, Beijing 100049, China
[3] National Laboratory of Biomacromolecules, CAS Center for Excellence in Biomacromolecules, Institute of Biophysics, Chinese Academy of Sciences, Beijing 100101, China
[4] Innovation Center of Optical Imaging and Detection Technology R&D, Bioland Laboratory (Guangzhou Regenerative Medicine and Health Guangdong Laboratory), Guangzhou 510320, China
[5] IDG/McGovern Institute for Brain Research, Tsinghua–Peking Joint Center for Life Science, School of Life Sciences, Tsinghua University, Beijing 100084, China
[6] Laboratory for Cell Adhesion and Tissue Patterning, RIKEN Center for Developmental Biology/RIKEN Center for Biosystems Dynamics Research, 650-0047 Kobe, Japan
[7] Innovation Academy for Seed Design, Chinese Academy of Sciences, Beijing 100101, China
[†] These authors contributed equally to this work.
* Correspondence to: Wei Ji, E-mail: jiwei@ibp.ac.cn; Xin Liang, E-mail: xinliang@tsinghua.edu.cn; Wenxiang Meng, E-mail: wxmeng@genetics.ac.cn

Edited by Xuebiao Yao

Microtubule networks support many cellular processes and exhibit a highly ordered architecture. However, due to the limited axial resolution of conventional light microscopy, the structural features of these networks cannot be resolved in three-dimensional (3D) space. Here, we used customized ultra-high-resolution interferometric single-molecule localization microscopy to characterize the microtubule networks in Caco2 cells. We found that the calmodulin-regulated spectrin-associated proteins (CAMSAPs) localize at a portion of microtubule intersections. Further investigation showed that depletion of CAMSAP2 and CAMSAP3 leads to the narrowing of the inter-microtubule distance. Mechanistically, CAMSAPs recognize microtubule defects, which often occur near microtubule intersections, and then recruit katanin to remove the damaged microtubules. Therefore, the CAMSAP–katanin complex is a regulatory module for the distance between microtubules. Taken together, our results characterize the architecture of cellular microtubule networks in high resolution and provide molecular insights into how the 3D structure of microtubule networks is controlled.

Keywords: CAMSAPs, microtubule intersections, microtubule networks

Introduction

Microtubule networks support multiple cellular functions, including intracellular transport, cell division, and directional migration (Toya and Takeichi, 2016; Bouchet and Akhmanova, 2017; Brouhard and Rice, 2018; Goodson and Jonasson, 2018). Although the structure and dynamics of microtubules have been extensively studied, much remains unknown about the structural characteristics and regulatory mechanisms of microtubule networks in cells due to the limited resolution of conventional optical microscopy, especially that in the z-axis.

The spatial distance between microtubules is an important characteristic of microtubule networks. In many cases, several microtubules bundle together to form compound structures, such as the spindle. However, in the interphase, microtubules stretch freely in the cell. It is intriguing how the spatial distribution of microtubules is regulated in cells. Intuitively, if the inter-microtubule distance is too narrow, the metabolic cost for

Received November 10, 2022. Revised March 14, 2023. Accepted August 10, 2023.

building and maintaining the network would be high, and the efficiency of intracellular transport might be hindered. The studies on the spatial distance between microtubules have focused on microtubule intersections (Bálint et al., 2013; Roll-Mecak, 2013). In plant cells, katanin, Spiral2, and augmin were reported to localize at microtubule intersections to regulate subsequent rearrangement processes (Wightman et al., 2013; Zhang et al., 2013; Wang et al., 2017, 2018). In mammalian cells, microtubules form complex three-dimensional (3D) networks that include numerous intersection sites (de Forges et al., 2016). However, quantitative characterization of the spatial distribution of microtubules has been impeded by the limited axial resolution of conventional optical microscopy. Therefore, little is known about how microtubules are spaced in cells.

In the present study, we used interferometric single-molecule localization microscopy (SMLM) (Gu et al., 2021), with the axial localization precision of ∼2 nm, to quantify the spatial distribution of microtubules and analyze how microtubule organization is regulated in cells. Our results showed that the spatial distribution of microtubules was not purely random but tightly regulated. Depletion of calmodulin-regulated spectrin-associated protein 2 (CAMSAP2) and CAMSAP3, two microtubule minus-end binding proteins (Meng et al., 2008; Tanaka et al., 2012; Akhmanova and Steinmetz, 2015), caused the narrowing of the inter-microtubule distance, possibly by impairing the CAMSAP–katanin module function. In addition, we showed that narrowing the inter-microtubule distance disrupted motor-driven directional transport, suggesting a functional contribution of CAMSAP2 and CAMSAP3 to maintaining an optimal network.

Results

The spatial organization of microtubule networks in cells

To determine the spatial organization of microtubule networks, we utilized homemade interferometric SMLM with improved resolution in the z-axis. The axial localization precision was ∼2 nm (see Materials and methods; Gu et al., 2021). We characterized the microtubule networks in fixed Caco2 epithelial cells, which were often used as a model to study cytoskeletal networks due to their relatively large sizes (Figure 1A).

Using the axial images of microtubules (Figure 1A and B), we measured the apparent diameter of individual microtubules and the z-axis distance between two microtubules that appeared to cross each other in 2D projection images, termed the inter-microtubule distance (Figure 1B–E). The results showed that the apparent diameter of a single microtubule was 48.5 ± 9.5 nm ($n = 89$ microtubules from three cells), larger than the known diameter of a microtubule (25 nm) (Figure 1D), which may reflect the expanding effect of the primary and secondary antibodies coated around the microtubules. The distribution of inter-microtubule distances peaked at 67.5 nm (Figure 1E). Although most of these 'intersecting' microtubules do not directly contact each other, we would still call such a structure 'intersection' in the following text for convenience.

CAMSAP2 and CAMSAP3 localize at microtubule intersections and regulate the inter-microtubule distance

In our studies on CAMSAPs, a family of proteins that decorate and stabilize non-centrosomal microtubule minus-ends (Meng et al., 2008; Akhmanova and Steinmetz, 2015), we noted that a portion of CAMSAPs were located at microtubule intersections in addition to associating with microtubule minus-ends (Figure 2A). Meanwhile, ∼40% of the microtubule intersections were positive for CAMSAP clusters within a distance of 0.3 μm from the intersection site, and no difference was found among CAMSAP1, CAMSAP2, and CAMSAP3 (Figure 2B). In addition, the probability of CAMSAPs appearing at microtubule intersections (∼40%) was significantly higher than the likelihood of co-occurrence determined by Monte Carlo simulations based on the purely random assumption (Figure 2B; de Forges et al., 2016). These observations suggest that CAMSAPs might be able to recognize or induce microtubule intersections.

To further understand how CAMSAPs bind to intersections, we first used SMLM to confirm that CAMSAP3, as a representative, is localized at microtubule intersections in addition to minus-ends (Figure 2C–E; Supplementary Video S1). Furthermore, we found that the CAMSAP3-positive intersections had a significantly shorter inter-microtubule distance than those without any CAMSAP3 signals (Figure 2F). This finding suggests that CAMSAP3 either narrows the inter-microtubule distance by cross-linking adjacent microtubules or preferentially localizes at intersections with a short inter-microtubule distance. Predictably, the inter-microtubule distance becomes larger in CAMSAP-depleted cells if CAMSAPs cross-link microtubules at intersections, or the inter-microtubule distance becomes smaller in CAMSAP-depleted cells if CAMSAPs preferentially land at shorter-distance intersections. To determine the mechanism, we studied CAMSAP2 and CAMSAP3-depleted cells (hereafter referred to as CAMSAP2+3 KD cells; Supplementary Figure S1A), as CAMSAP2 and CAMSAP3 function synergistically in the organization and stabilization of non-centrosomal microtubules (Tanaka et al., 2012; Akhmanova and Steinmetz, 2015). The most prominent change observed in CAMSAP2+3 KD cells was that the percentage of microtubule intersections with a distance <50 nm (i.e. an actual lattice-to-lattice distance of 25 nm) was significantly increased in comparison to that in control cells (Figure 2H). Moreover, the distribution of inter-microtubule distances in CAMSAP2+3 KD cells peaked at 52.1 ± 2.8 nm, which was significantly smaller than that in control cells (69.9 ± 11.4 nm) (Figure 2I). These results support that CAMSAPs are able to recognize short-distance pairs of microtubules rather than acting as microtubule cross-linkers. We also measured the acute angles of all microtubule intersections and CAMSAP-positive intersections but did not find any correlation between the intersection angle and the localization of CAMSAPs (Figure 2G).

CAMSAPs localize at microtubule intersections by recognizing damaged sites on microtubules

To further analyze the dynamics of CAMSAP clusters, we performed live-cell imaging (Figure 3A; Supplementary Video S2).

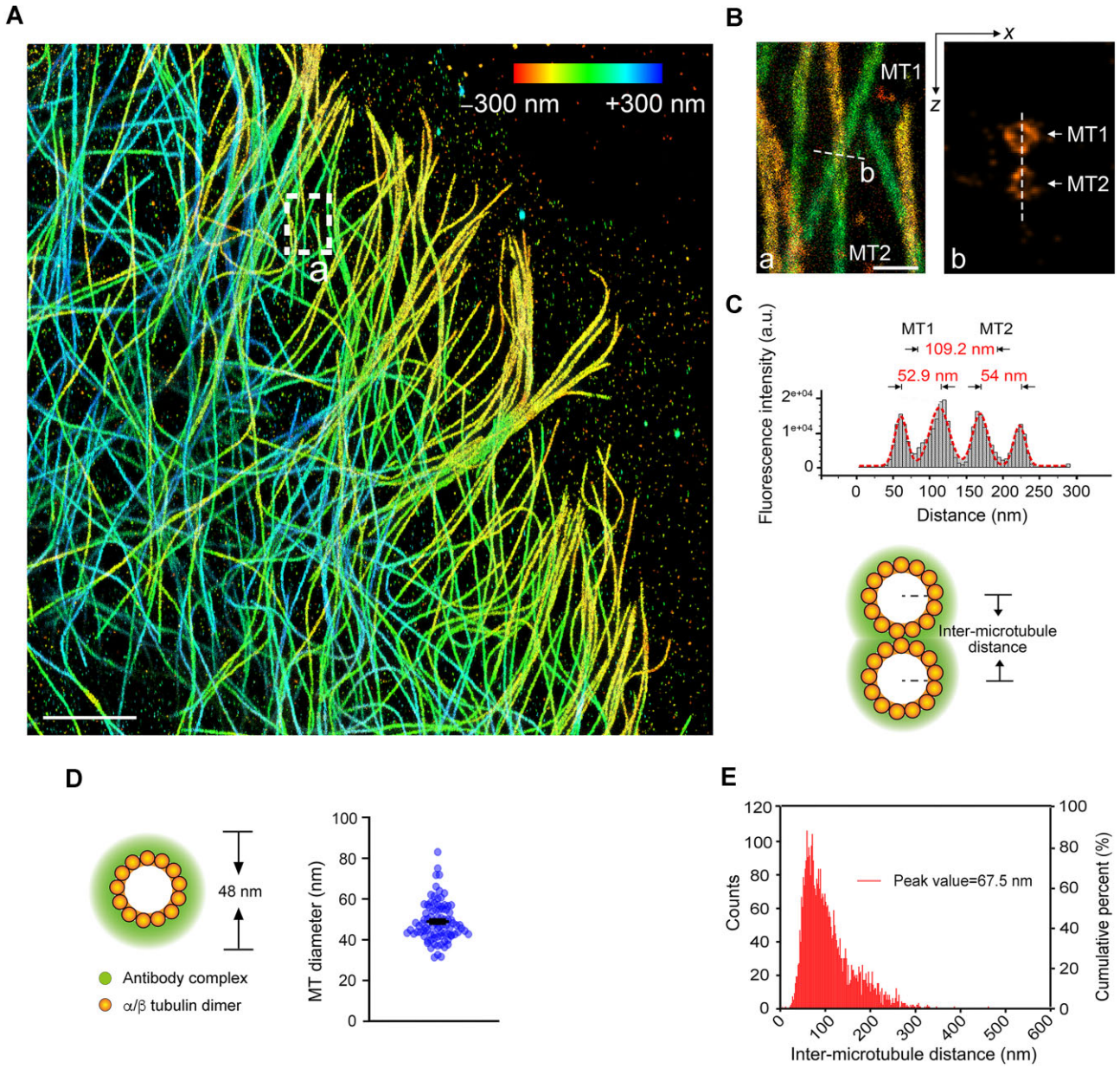

Figure 1 Microtubule spatial organization is regulated in cells. (**A**) 3D SMLM image of microtubules in Caco2 cells. Scale bar, 5 μm. (**B**) The boxed region in **A** is enlarged in **B-a**. The X–Z plane of the microtubule intersection site in **B-a** is shown in **B-b**. Scale bar, 500 nm. MT, microtubule. (**C**) A sample graph of using Gaussian fitting to calculate the inter-microtubule distance in **B-b**. (**D**) A diagrammatic model of the apparent diameter of the microtubule. The scatter diagram shows the diameter of individual microtubules measured from the 3D SMLM images ($n = 89$ from three cells). Data are presented as mean ± SEM. (**E**) Histograms show the distribution pattern of inter-microtubule distances measured from the 3D SMLM images. The peak value was calculated by the inflection point of the cumulative probability curve ($n = 4231$ from six cells).

Time recording analysis showed that green fluorescent protein (GFP)-tagged CAMSAPs appeared at microtubule crossings with an average latency of 9.5 sec for CAMSAP1, 8.2 sec for CAMSAP2, and 8.0 sec for CAMSAP3 (Figure 3B). These data indicate that the localization of CAMSAP clusters at microtubule crossings is a subsequent event after the formation of the crossings, confirming that CAMSAPs recognize microtubule intersections rather than mediating their formation (e.g. by acting as cross-linkers). CAMSAP3 clusters showed similar dynamics at the intersection sites (Supplementary Video S3) as CAMSAP1.

Previous studies indicated that lattice damage on microtubules is more likely observed near intersection sites both *in vivo* and *in vitro* (Aumeier et al., 2016; de Forges et al., 2016). In addition, CAMSAPs can recognize the C-terminal of exposed

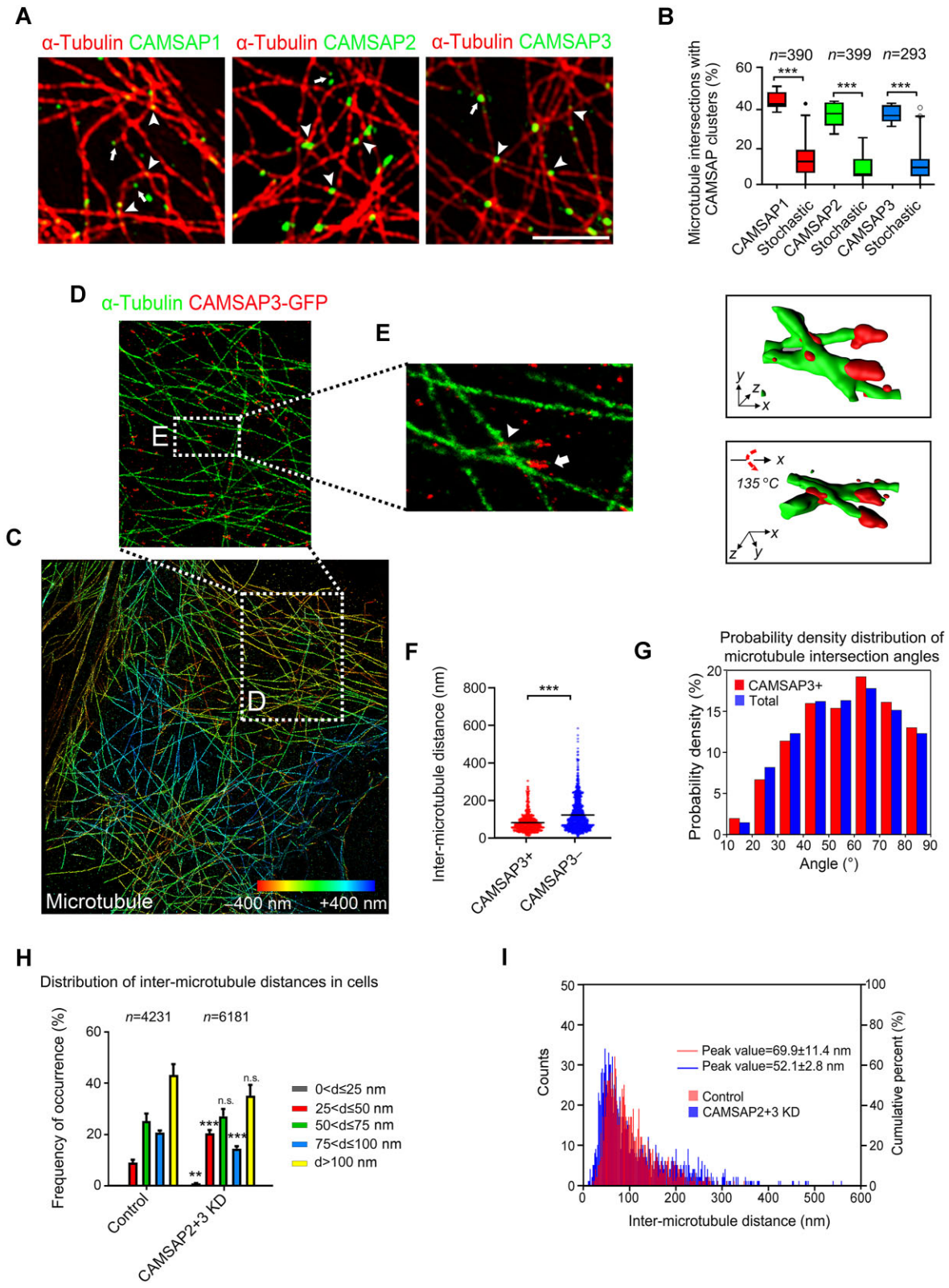

Figure 2 CAMSAPs localize at microtubule intersections in mammalian cells and regulate the distribution of inter-microtubule distances. (**A**) Caco2 cells were fixed and processed for immunolabelling of CAMSAP1, CAMSAP2, or CAMSAP3 along with α-tubulin. Arrowheads and arrows indicate CAMSAP clusters that localize at microtubule intersections and minus-ends, respectively. Scale bar, 2 μm. (**B**) Boxplots show the percentages of microtubule intersections positive for CAMSAP clusters within a distance of 0.3 μm from the intersection site in Caco2 cells and

α-tubulin at open microtubule structures (Atherton et al., 2017). Thus, CAMSAPs might bind to intersection sites by recognizing lattice damage.

To test this hypothesis, we first examined whether lattice damage occurs when two microtubules encounter each other *in vitro*. Using transmission electron microscopy (TEM) and taxol-stabilized microtubules, we observed nanoscale damages at 18% of the intersection sites (Figure 3C). The likelihood of damage occurrence on the microtubule lattice or intersections was quantified (Supplementary Figure S1B). Our results showed a higher damage frequency when two microtubules made direct contact (Figure 3D).

Next, we checked whether CAMSAPs preferentially bind to damaged sites on microtubules. Katanin, a microtubule-severing enzyme, consists of two subunits, p60 and p80. We then purified CAMSAPs, katanin p60, and the RFP-katanin p80 C-terminal domain (p80C) (Supplementary Figure S2A). The purified N-terminal GFP-tagged CAMSAPs could track microtubule minus-ends *in vitro*, consistent with previous reports and demonstrating that the purified CAMSAPs were functional (Supplementary Figure S2B and Video S4; Hendershott and Vale, 2014; Jiang et al., 2014). The purified katanin was used to create nanoscale damage on the microtubule lattice (Figure 3E; Jiang et al., 2017; Vemu et al., 2018). To avoid interference from the katanin–microtubule interaction, we studied the localization of CAMSAP1 on damaged microtubules, since it does not interact with katanin. It was reported that the localization of CAMSAP2 and CAMSAP3 on the microtubule lattice is due to their interaction with katanin rather than their localization with damaged microtubules (Jiang et al., 2014, 2018). We observed the accumulation of GFP-CAMSAP1 in numerous clusters along the damaged microtubules, while in the absence of katanin, GFP-CAMSAP1 was only observed at the minus-ends of microtubules (Figure 3F and G). These results demonstrate that CAMSAPs can recognize damaged sites in the microtubule lattice.

Finally, we examined whether the damaged sites are associated with microtubule intersections in cells (de Forges et al., 2016). To this end, we labelled GTP-tubulin islands with the hMB11 antibody (Figure 3H and I; Dimitrov et al., 2008). We found that ∼50% of the microtubule intersections were positive for GTP-tubulin. The proportion of GTP-tubulin-positive intersections was significantly higher than random co-occurrence (Figure 3J), confirming a higher damage frequency at the intersection sites. Furthermore, we found that ∼24% of the microtubule intersections were positive for both GTP-tubulin and CAMSAP2 signals (Figure 3K), which are likely damaged sites that are not yet fully repaired. These results confirm our hypothesis that CAMSAPs bind to damaged sites on microtubules, through which they could recognize microtubule intersections.

CAMSAP2 and CAMSAP3 recruit katanin to sever at microtubule intersections

CAMSAP2 and CAMSAP3 were known to be able to recruit katanin, and the CAMSAP–katanin module could regulate the length of CAMSAP-decorated microtubule stretches (Jiang et al., 2014, 2018). Therefore, we wondered whether the CAMSAP–katanin module could eliminate damaged microtubules, i.e. reducing the number of short-distance microtubule intersections but not that of far-distance intersections.

First, we examined whether CAMSAP2 and CAMSAP3 promote severing efficiency by recruiting katanin onto microtubules. Given that CAMSAP2 and CAMSAP3 function in cells in a similar manner (Tanaka et al., 2012; Akhmanova and Steinmetz, 2015), CAMSAP3 was tested as a representative. We pre-incubated microtubules with a high concentration (100 nM) of CAMSAP3, which decorates the microtubule lattice, or CAMSAP1 that does not interact with katanin as a negative control before katanin treatment (Figure 4A and B; Supplementary Video S5). The severing efficiency of katanin at the microtubule lattice was significantly increased in the CAMSAP3-pretreated microtubules compared with the CAMSAP1-pretreated microtubules. Thus, CAMSAP3 promotes the severing efficiency by facilitating the recruitment of katanin onto microtubules.

Next, we examined how CAMSAPs regulate the severing of microtubule intersections in cells. To visualize the co-localization sites of CAMSAP3 and katanin in Caco2 cells, katanin p60-GFP was expressed and co-immunostained with CAMSAP3. In interphase Caco2 cells, katanin exhibited diffused subcellular localization (Supplementary Figure S2C),

Figure 2 *(Continued)* the stochastic distributions determined by Monte Carlo simulations. For CAMSAP1, CAMSAP2, and CAMSAP3 location, $n = 390$, 399, and 293 intersections from eight cells, respectively. For the Monte Carlo simulation, $n = 200$ cycles. The whiskers show the 1st and 99th percentiles. (**C**–**E**) A representative interferometric 3D SMLM image of microtubules in Caco2 cells. The boxed region in **C** is enlarged in **D**. The boxed region in **D** is enlarged in **E**. Pseudo colors are added to show α-tubulin in green and CASMAP3-GFP in red. The arrowhead and arrow indicate CAMSAP3 clusters that localize at the microtubule intersection and the minus-end, respectively. Right panel: reconstructed images showing CAMSAP localization at microtubule minus-ends and intersections. (**F**) Scatter diagrams show the inter-microtubule distances with (+) or without (–) CAMSAP3 signals. Data are presented as mean ± SEM. (**G**) Histograms show the probability density distributions of total and CAMSAP3-positive microtubule intersection angles in cells. For CAMSAP3+, CAMSAP3−, and Total groups, $n = 675$, 1085, and 1760 intersections from three cells, respectively. (**H**) Histograms show the distribution percentages of different inter-microtubule distances in control cells ($n = 4231$ intersections from six cells) and CAMSAP2+3 KD cells ($n = 6181$ intersections from six cells). Data are presented as mean ± SEM. (**I**) Histograms show the distribution patterns of inter-microtubule distances from a representative control cell ($n = 1112$ intersections) and a representative CAMSAP2+3 KD cell ($n = 1321$ intersections). The peak value of inter-microtubule distances was calculated by the inflection point of the cumulative probability curve. Data are presented as mean ± SEM. Asterisks represent significant differences as calculated by two-tailed Student's *t*-test: n.s., $P > 0.05$; $^{**}P < 0.01$; $^{***}P < 0.001$.

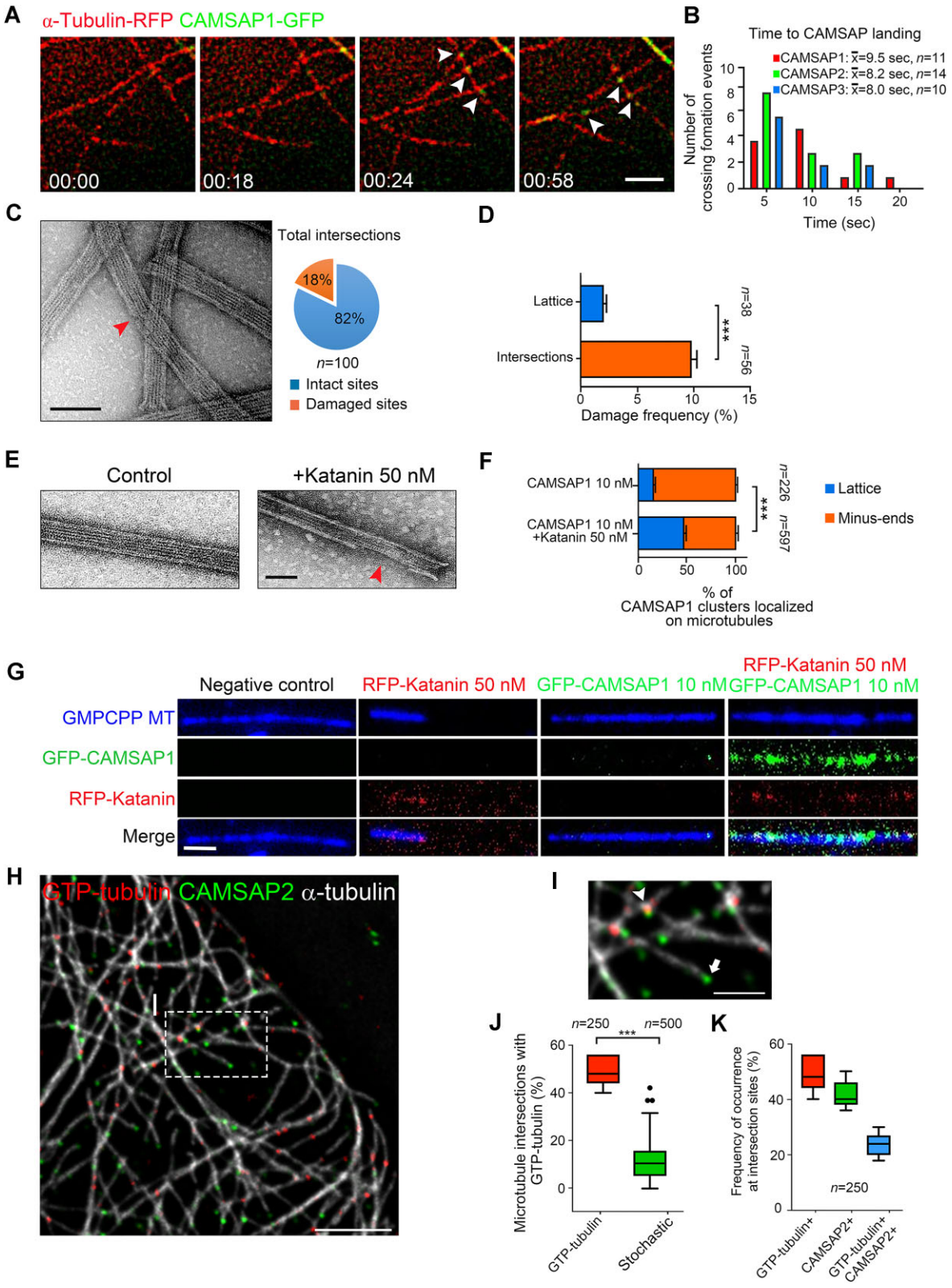

Figure 3 CAMSAPs localize at microtubule intersections by recognizing damaged sites. (**A**) Cos7 cells expressing CAMSAP1-GFP and α-tubulin-RFP were recorded. Arrowheads indicate CAMSAP1 clusters that localize at intersections. Scale bar, 2 μm. (**B**) Histograms show the time from microtubule intersection formation to the recruitment of CAMSAP clusters ($n > 10$ CAMSAP-positive intersections from five cells). (**C**) Left panel: a representative TEM image of damaged microtubule intersections. Microtubules were imaged at 250000× magnification.

consistent with the previous report (Jin et al., 2017). Despite this, time-lapse recording of microtubules (α-tubulin-GFP) and CAMSAP3-RFP showed that one microtubule at the intersection was cut and depolymerized after the CAMSAP3 cluster appeared at the intersection (Figure 4C; Supplementary Video S6). This observation may provide insights into the dynamic nature of katanin binding with CAMSAPs and microtubules. Further statistical quantification showed that the likelihood of a microtubule being severed was higher at CAMSAP3-positive intersections than at CAMSAP3-negative or CAMSAP1-positive intersections, though CAMSAP1 and CASMAP3 have similar landing frequencies at microtubule intersections (28.6% ± 8.8% for CAMSAP1 and 28.3% ± 12% for CAMSAP3) (Figure 4B and D). Approximately 9.7% of the microtubules were severed and depolymerized at CAMSAP3-positive microtubule intersections, while no severing events were observed at CAMSAP1-positive intersections (Figure 4E). Therefore, CAMSAP3, but not CAMSAP1, promotes the elimination of microtubule intersections.

Finally, if katanin works as a part of the CAMSAP–katanin module, depletion of katanin is expected to change the cellular distribution of inter-microtubule distances in cells similarly as loss of CAMSAPs. Using SMLM, we found a significantly increased proportion of short-distance (≤50 nm) microtubules and the smaller peak value at 52.2 ± 2.6 nm in katanin p60 KD cells (Figure 4F and G; Supplementary Figure S2D), similar to that observed in CAMSAP2+3 KD cells.

Knockdown of CAMSAP2 and CAMSAP3 or katanin alters lysosomal transport

We wondered how optimal microtubule networks would contribute to the efficiency of intracellular transport. Intuitively, overcrowding of microtubules might impede motor motility and in turn affect the motor-driven direction of transport. It has been shown that motor proteins pause, switch, and reverse at microtubule intersections if the separation distance is small (Bálint et al., 2013; Bergman et al., 2018). Therefore, we examined the intracellular transport in CAMSAP2+3 KD and katanin p60 KD cells by analyzing lysosome motility (Supplementary Figure S3A and Video S7). We calculated the α-coefficient for the mean-square displacement curve of each vesicle by fitting the data to a power-law, $\log[\mathrm{MSD}(\Delta t)] = \alpha \log[(\Delta t)] + C$. In this model, $\alpha \leq 1$ and $\alpha > 1$ represent subdiffusive/diffusive and processive motion, respectively (Supplementary Figure S3B; Bálint et al., 2013; Bergman et al., 2018). We found that the occurrence of directional movement ($\alpha > 1$) decreased in CAMSAP2+3 KD and katanin p60 KD cells in comparison to that in control cells (Supplementary Figure S3C). However, the moving velocity of the lysosome did not significantly change in CAMSAP2+3 KD and katanin p60 KD cells, suggesting that the motility of motor proteins is unchanged (Supplementary Figure S3D).

Furthermore, we specifically analyzed lysosome behaviors at microtubule intersections with different inter-microtubule distances by correlating the data from the live-cell imaging experiments to those from the SMLM super-resolution imaging (Supplementary Figure S3E; Bálint et al., 2013). By tracking the trajectories of lysosomes at microtubule intersections, we classified lysosome behaviors into three types: pass, switch, and reverse. Then, we measured the average inter-microtubule distance of the intersections where each type of lysosome movement occurs. We found that the pass, switch, and reverse events occurred at the intersections with axial separations of 210.7 ± 88.9 nm, 71.6 ± 26.3 nm, and 52.6 ± 17.1 nm, respectively (Supplementary Figure S3F and G), demonstrating that directional movements are more likely to be observed when two microtubules are widely separated. In addition, the switch and reverse events in lysosomes occurred more frequently in CAMSAP2+3 KD and katanin p60 KD cells than in control cells (Supplementary Figure S3H).

Figure 3 *(Continued)* The red arrowhead indicates a nanoscale damaged site around the microtubule intersection. Scale bar, 50 nm. Right panel: the tortadiagram shows the proportions of damaged and intact sites in total intersections ($n = 100$ intersections). (**D**) Histograms show the damage frequencies at the microtubule lattice ($n = 56$ microtubules from five TEM images) and intersections ($n = 38$ microtubules from five TEM images). The intersection damage frequency was defined as the ratio of damaged intersection area to total intersection area, and the lattice damage frequency was defined as the ratio of damaged lattice area to total microtubule area (illustrated in Supplementary Figure S1B). Data are presented as mean ± SEM. (**E**) Representative TEM images of control and 50 nM katanin-treated microtubules. Taxol-stabilized microtubules showing nanoscale damaged sites on the microtubule lattice (red arrowhead). Scale bar, 50 nm. (**F**) Histograms show the percentages of CAMSAP1 clusters located at the microtubule lattice and minus-ends in the presence or absence of 50 nM katanin. Data are presented as mean ± SEM. (**G**) Taxol-stabilized microtubules were assembled *in vitro* and then incubated with 50 nM katanin, 10 nM GFP-CAMSAP1, or both with 1 mM ATP. Representative images are shown. Scale bar, 2 μm. (**H** and **I**) Caco2 cells were fixed and processed for immunolabelling of GTP-tubulin, CAMSAP2, and α-tubulin. A representative image is shown in **H**. The boxed region is enlarged in **I**. The arrowhead and arrow indicate CAMSAP2 clusters that colocalize with GTP-tubulin islands at microtubule intersections and localize at microtubule minus-ends, respectively. Scale bar, 5 μm (**H**) and 2 μm (**I**). (**J**) Boxplots show the percentage of microtubule intersections positive for GTP-tubulin and stochastic distribution determined by Monte Carlo simulations. For GTP-tubulin location, $n = 250$ intersections from five cells; for the Monte Carlo simulation, $n = 500$ cycles. The whiskers show the 1st and 99th percentiles. (**K**) Boxplots show the percentage of microtubule intersections positive for GTP-tubulin, CAMSAP2 clusters within a distance of 0.3 μm from the intersection site, or both in Caco2 cells. $n = 250$ intersections from five cells. The whiskers show the 1st and 99th percentiles. Asterisks represent significant differences as calculated by two-tailed Student's *t*-test: $^{***}P < 0.001$.

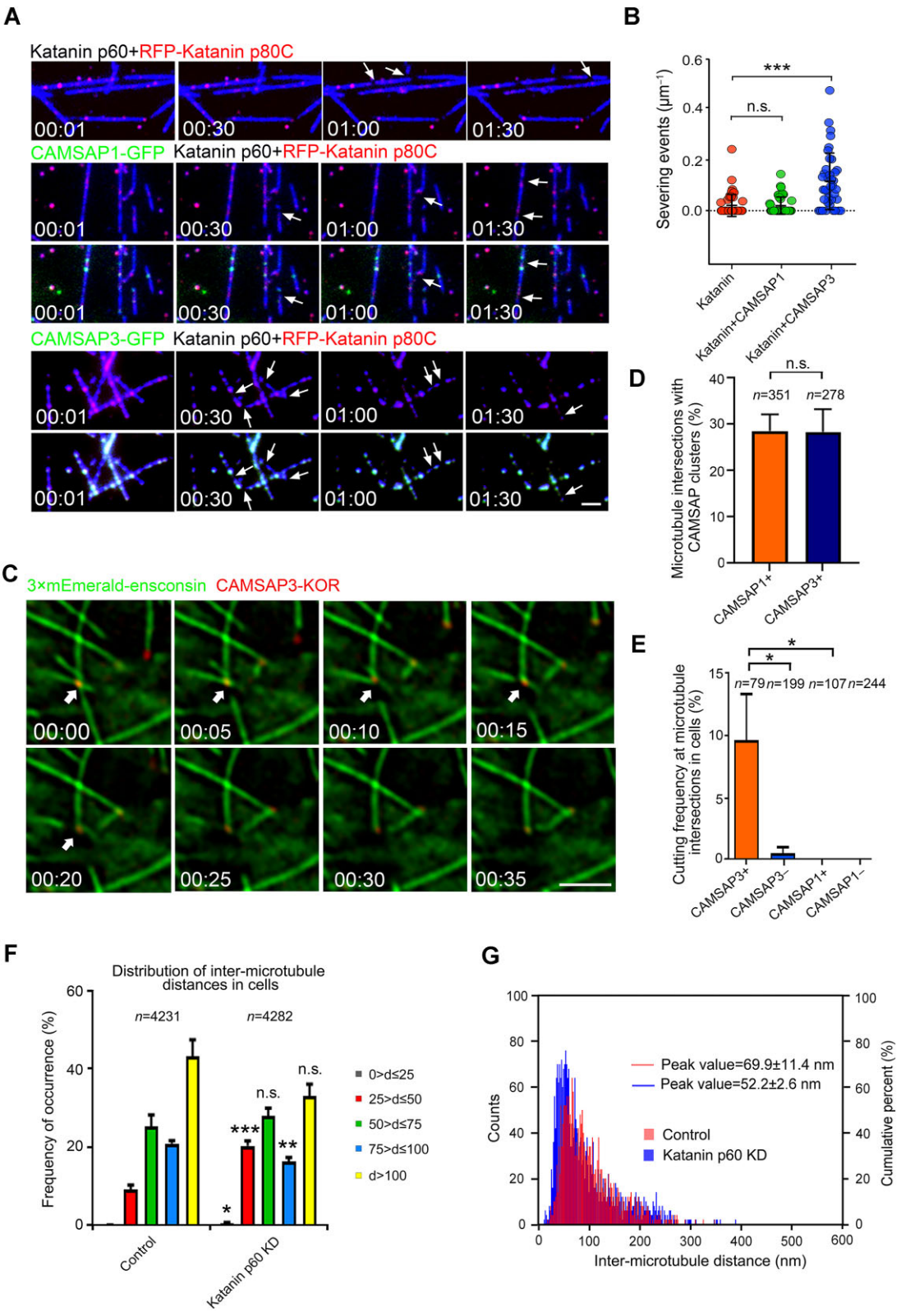

Figure 4 CAMSAP2 and CAMSAP3 recruit katanin to microtubule intersections. (**A**) Taxol-stabilized microtubules were incubated with 100 nM katanin in the absence or presence of pre-incubation with 100 nM CASMAPs. Images were obtained by TIRF microscopy. Arrows indicate katanin-induced severing events. Scale bar, 2 μm. (**B**) Scatter diagrams show the severing efficiency of katanin at the microtubule lattice in the

The same results were obtained from analyzing the mobility of another intercellular transport cargo, membrane-type 1 matrix metalloprotease (MT1-MMP, also known as MMP-14), which is targeted to focal adhesions and mediates local extracellular matrix (ECM) degradation near focal adhesions (Supplementary Figure S4A–D). More diffusive/subdiffusive motions were found in CAMSAP2+3 KD and katanin p60 KD cells (Supplementary Figure S4A and B). The focal adhesion area became relatively larger due to inefficient ECM degradation near focal adhesions (Supplementary Figure S4C and D). Because the total number of microtubules in the cellular network could also affect the density of microtubules and in turn alter the efficiency of intracellular transport, we measured the total fluorescence intensity of microtubules in cells. However, the total mass of microtubules did not change significantly in CAMSAP2+3 KD or katanin p60 KD cells compared to control cells (Supplementary Figure S4E and F), suggesting that the redistribution of microtubule spatial arrangement is not likely due to the change in the number of microtubules. In summary, these results demonstrate that an optimal inter-microtubule distance facilitates efficient intracellular transport.

Discussion

With the development of super-resolution optical microscopy, the regulation of microtubule spatial distribution has gradually entered the spotlight, but there are only a few studies so far that have shed light on the intersections of microtubules in mammalian cells (Liu et al., 2014). Our study used ultra-high-resolution SMLM to quantify and analyze the distribution of inter-microtubule distances in cultured cells. The results show that the arrangement of microtubules in space is not random but regulated by cellular mechanisms.

Our findings have revealed a molecular mechanism that regulates the microtubule spatial organization in cells. CAMSAPs could directly identify microtubule lattice damage, which occurs more often when microtubules are getting too close. Having recognized microtubule lattice sites, CAMSAPs could then recruit the severing enzyme katanin to increase the severing frequency at these defective sites, thereby regulating the spatial distribution of microtubules (Figures 3E–K and 4; Supplementary Video S6). In this process, lattice damages on microtubules play an essential role. The cause of these damaged sites at intersections could be attributed to the local mechanical stress due to physical contact (Aumeier et al., 2016; de Forges et al., 2016).

Other factors may also contribute to mechanical stress, such as motors or bundling proteins (Doodhi et al., 2014; Ahmadzadeh et al., 2015). A recent study showed that in CAMSAP2-depleted cells, microtubules exhibit more self-repaired sites and less efficient intercellular transport (Hao et al., 2020). These data are consistent with our findings. However, there are still many open questions regarding this process, e.g. it is not clear whether other microtubule-severing enzymes are also involved in regulating microtubule intersections. These issues await future studies.

Why does microtubule spatial organization need to be controlled in cells? The wide distribution of microtubule intersections indicates that their impact on the function of microtubule networks is extensive (Goodson and Jonasson, 2018). When the spatial distance between two adjacent microtubules is $<$100 nm (the resolution of conventional 3D-STORM in the axial), the microtubule intersection might have a significant impact on intracellular transport, because the directional movement of motor proteins is hindered (Bálint et al., 2013; Bergman et al., 2018). Our results indicate that depletion of CAMSAP2, CAMSAP3, and/or katanin p60 could cause the narrowing of inter-microtubule distances and in turn decrease the efficiency of intercellular transport. These phenomena demonstrate the importance of microtubule density in optimizing intracellular transport.

Materials and methods

Plasmids, antibodies, and siRNAs

CAMSAP1, CAMSAP2, and CAMSAP3 were cloned into the pOCC6_pOEM1-N-HIS6-EGFP vector, and katanin p80C was cloned into the pOCC18_pOEM1-N-HIS6-RFP vector. Mouse katanin p80C and katanin p60 sequences were obtained by PCR from katanin p80C-GFP and katanin p60-no tag, which were kindly gifted by Dr Kai Jiang (Wuhan University). Katanin p60 was cloned into pOCC18_pOEM1-N-HIS6-RFP deleted of TagRFP and 6×His tag. The 3×mEmerald-ensconsin plasmid was used to visualize microtubules in cells, which was a kind gift from Dr Dong Li (Institute of Biophysics, Chinese Academy of Sciences)

Figure 4 *(Continued)* absence ($n = 51$ microtubules) or presence of CAMSAP1 ($n = 41$ microtubules) or CAMSAP3 ($n = 37$ microtubules). Three independent experiments were performed. (**C**) Microtubules were visualized in Caco2 cells expressing CAMSAP3-KOR and 3×mEmerald-ensconsin at the indicated time points. Arrows indicate that the microtubule intersection is cut after the CAMSAP3 signal appears. Scale bar, 2 μm. (**D**) Histograms show the percentages of microtubule intersections positive for CAMSAP1 ($n = 351$ intersections from six cells) and CAMSAP3 ($n = 278$ intersections from six cells) in live Caco2 cells. (**E**) Histograms show the cutting frequencies at microtubule intersections in the indicated cells. For CAMSAP3+, CAMSAP3−, CAMSAP1+, and CAMSAP1− groups, $n = 79$, 199, 107, and 244 intersections from six cells, respectively. (**F**) Histograms show the percentages of different inter-microtubule distances in control cells ($n = 4231$ intersections from six cells) and katanin p60 KD cells ($n = 4282$ intersections from six cells). (**G**) Histograms show the distribution patterns of microtubule intersection distances from a representative control cell ($n = 1112$ intersections) and a representative katanin p60 KD cell ($n = 1326$ intersections). The peak value of inter-microtubule distances was calculated by the inflection point of the cumulative probability curve. Data are presented as mean ± SEM. Asterisks represent significant differences as calculated by two-tailed Student's *t*-test: n.s., $P > 0.05$; *$P < 0.05$; **$P < 0.01$; ***$P < 0.001$.

(Guo et al., 2018). α-tubulin-RFP, α-tubulin-GFP, CAMSAP2-KOR, CAMSAP3-KOR, CAMSAP1-GFP, GAMSAP2-GFP, CAMSAP3-GFP, and katanin p60-GFP were cloned in our laboratory.

Guinea pig polyclonal anti-CAMSAP1 was generated by Zhou et al. (2020). Rabbit polyclonal anti-CAMSAP2 was purchased from ProteinTech. Rabbit polyclonal anti-CAMSAP3 was generated as described before (Meng et al., 2008). Mouse monoclonal anti-α-tubulin (clone DM1A) was purchased from Sigma. Rabbit polyclonal anti-GFP was purchased from MBL. All secondary antibodies for immunostaining were purchased from Invitrogen. GTP-tubulin antibody hMB11 was purchased from AdipoGen.

All the siRNAs used in this study are summarized in Supplementary Table S1.

Immunostaining

For most of immunostaining experiments, cells were fixed with ice-cold methanol for 5 min at −20°C, then washed three times with phosphate-buffered saline (PBS) containing 0.1% Triton X-100 and incubated for 30 min with 1% bovine serum albumin (BSA; AMRESCO) at room temperature. Cells were incubated with primary antibodies for 1 h and secondary antibodies for 1 h. Coverslips were mounted in FluorSave reagent (Millipore).

For GTP-tubulin labelling experiments, cells were permeabilized at 37°C in PEM buffer (80 mM Pipes–KOH, 2 mM EGTA, 1 mM $MgCl_2$, pH 6.9) supplemented with 10% glycerol, 0.1% Triton X-100, and 1 μM Taxol for 3 min. Then, cells were incubated with hMB11 for 15 min at 37°C in PEM–glycerol containing 0.2% BSA and 1 μM taxol, followed by short washes with PEM–glycerol–taxol–BSA. Subsequently, cells were incubated with a secondary antibody for 10 min in PEM–glycerol–taxol–BSA for 10 min at 37°C and washed three times. For co-labelling, cells were fixed in cold methanol (−20°C for 5 min) and stained with specific antibodies.

For 3D SMLM imaging, cells were fixed with pre-warmed PBS containing 2% (*v*/*v*) paraformaldehyde and 0.1% glutaraldehyde at 37°C for 10 min and washed twice with PBS. For two-color 3D SMLM imaging, cells were fixed with pre-warmed PBS with 2% (*v*/*v*) paraformaldehyde and 0.01% glutaraldehyde at 37°C for 10 min. The background fluorescence of glutaraldehyde was quenched by incubating cells with 0.1% $NaBH_4$ in PBS for 7 min at room temperature. Then, cells were washed with PBS three times and permeabilized with 0.2% Triton X-100 in PBS for 15 min. Subsequently, cells were incubated for 90 min blocking with PBS containing 10% normal goat serum (NGS) and 0.05% Triton X-100 at room temperature, immunostained with primary antibodies (diluted with PBS containing 5% NGS and 0.05% Triton X-100) for 1 h, washed with washing buffer (1% NGS and 0.05% Triton X-100 in PBS) five times (15 min per wash), and incubated with secondary antibodies for 60 min. Cells were washed with PBS for 5 min after being washed with washing buffer. PBS containing 2% paraformaldehyde and 0.1% glutaraldehyde was used to post-fix cells for 10 min. Cells were then washed with PBS three times (5 min per wash). Finally, cells were washed with ddH_2O twice (3 min per wash) and saved with ddH_2O at 4°C.

For two-color microtubule–CAMSAP3 SMLM samples, the CAMSAP3-GFP plasmid was expressed in Caco2 cells. The mouse anti-α-tubulin antibody was diluted to 1:50, and the rabbit anti-GFP antibody was diluted to 1:250. The secondary antibody CF660C donkey anti-mouse IgG (Biotium) was diluted to 1:10, and Alexa Fluor 647 goat anti-rabbit IgG was diluted to 1:50.

Live-cell imaging, image processing, and statistical analysis

Cells were plated on glass-bottomed cell culture dishes (Nest) and transfected with the indicated plasmids. LysoTracker Red DND *99* (Invitrogen) was added to the culture medium at a final concentration of 1 μM for 20 min at 37°C for lysosomal staining in live cells. Fluorescence images were taken by a Delta Vision microscope (Applied Precision) at 37°C, 5% CO_2 using a 100× objective. For immunostaining of CAMSAPs and microtubules in Caco2 cells, images were obtained through a GE Healthcare structured illumination microscope (Delta Vision OMX V4) equipped with the sCMOS camera (pco.edge).

Kymography, 3D projection, and image analysis were conducted using ImageJ. Lysosome tracking was performed by the Imaris particle tracking function and mean-square displacement (MSD), which is a measure of the deviation of the position of a particle with respect to a reference position over time. The speed and displacement of lysosomes were also quantified by Imaris. Lysosome α-coefficients for mean-square displacement curves were calculated for each lysosome by fitting to a power law, $\log[\mathrm{MSD}(\Delta t)] = \alpha \log[(\Delta t)] + C$, and performed by Excel. Subdiffusive, diffusive, and part processive/part diffusive motions are given by $\alpha < 1$, $\alpha = 1$, and $\alpha > 1$, respectively. For lysosome behavior analysis at microtubule intersections, lysosomes were tracked by the ImageJ MTrackJ plugin, and switch and reverse paths were counted in each experimental group. For calculating the distance between two microtubules at the intersection, we measured the fluorescence intensity value of axial microtubule images at intersections. Then, Gaussian fitting was used to calculate the center of each microtubule by MATLAB (MathWorks R2020a), and the distance of microtubule intersection was obtained by the deviation of the coordinate center of the X-axis of the fitting curves (Figure 1D). Comparisons were performed by two-tailed Student's *t*-test using Origin or GraphPad Prism. Data are presented as mean ± standard error of the mean (SEM). All experiments were performed with at least two biological replicates.

Live-cell movie and SMLM image correlation

To determine the correlation of live-cell movies with SMLM images, we used a 35-mm glass-bottomed dish with a 14-mm micro-well #1.5 gridded (Cellvis) to plate cells. After movie recording, the cells were fixed with pre-warmed PBS containing 2% (*v*/*v*) paraformaldehyde and 0.1% glutaraldehyde for 10 min and then washed three times with PBS for immunostaining. Images were acquired at 1-sec intervals for 1 min. Lysosome tracking was performed by the Imaris particle tracking function. Lysosome trajectories were extracted and merged with the final frames of time-lapse movies and SMLM images.

Randomness test

The Monte Carlo simulation of stochastic CAMSAP cluster distribution was performed by a short program developed in Python. First, we assumed that microtubule intersections were located randomly across a 20 μm-long microtubule according to the frequency measured in cells. Second, we assumed that CAMSAP clusters were distributed randomly along the microtubule. The percentage of CAMSAP clusters that colocalized with microtubule intersections (within a radius of 0.1 μm) was calculated after counting at least 200 microtubule intersections.

To calculate the peak value of microtubule intersection distances in Caco2 cells, the cumulative probability curve of microtubule intersection distances was fitted to get the fitting formula, and then the inflection point of the fitting formula was worked out.

SMLM imaging and data analysis

The interferometric SMLM imaging was performed with a custom-built super-resolution microscope on an Olympus IX71 inverted microscope and a 100× 1.5 NA oil-immersion objective. The microscope utilized interferometric fringes to achieve an ultra-high z-axis resolution, which is similar to that reported for lateral resolution improvement (Gu et al., 2019). A 639-nm laser was used for excitation of Alexa Fluor 647 and CF 660C, and a 405-nm laser was used for activation and control of the molecule intensity during image acquisition. Images were acquired on an Andor iXon DU-897 EMCCD camera, and the pixel size was 150 nm with a field of view of ∼ 30 μm × 30 μm. An active drift correction method was used to correct mechanical drift during image acquisition.

For SMLM data acquisition, an exposure time of 50 ms, an EM gain of 20, and an illumination power intensity of ∼4 kW/cm^2 were used. A total of 400000 frames were acquired for the super-resolution image reconstruction. During imaging, the 405-nm laser was used to control the molecule density.

The sample was sealed between two coverslips to create a sandwich structure for imaging, with imaging buffer, i.e. 10% glucose, oxygen removed, GLOX (0.6 mg/ml glucose oxidase and 0.06 mg/ml catalase dissolved in Tris–HCl buffer), and 143 mM 2-mercaptoethanol in PBS, filled in the chamber to enable blinking of the dyes during imaging. Sample drift during acquisition was calculated by reconstructing STORM images from subsets of frames and correlating images to a reference frame.

Supplementary material

Supplementary material is available at *Journal of Molecular Cell Biology* online.

Acknowledgements

We thank Dr Kai Jiang (Wuhan University) for providing the katanin plasmids, S. Zhang and Y. Li for assisting with interferometric SMLM sample preparation, Dr Dong Li (Institute of Biophysics, Chinese Academy of Sciences) for providing the 3×mEmerald-ensconsin plasmid, L. Yang for assisting with TEM microscopy, and J. He for building a theoretical stochastic model of microtubule intersection distance distribution.

Funding

This work was funded by the National Natural Science Foundation of China (31930025, 31922018, and 3227073) and the National Key Research and Development Program of China (2021YFA0804802 and 2018YFA0801104). X.L. was supported by the IDG/McGovern Institute for Brain Research at Tsinghua University.

Conflict of interest: none declared.

Author contributions: R.Z., W.J., X.L., and W.M. designed all the experiments, interpreted the results, and prepared the manuscript. R.Z. and H.X. analyzed the data. R.Z. performed microtubule-binding assays with the help of W.C. and X.L. X.L. provided reagents and advice. L.G., T.X., and W.J. performed interferometric SMLM imaging and image reconstruction.

References

Ahmadzadeh, H., Smith, D.H., and Shenoy, V.B. (2015). Mechanical effects of dynamic binding between Tau proteins on microtubules during axonal injury. Biophys. J. *109*, 2328–2337.

Akhmanova, A., and Steinmetz, M.O. (2015). Control of microtubule organization and dynamics: two ends in the limelight. Nat. Rev. Mol. Cell Biol. *16*, 711–726.

Atherton, J., Jiang, K., Stangier, M.M., et al. (2017). A structural model for microtubule minus-end recognition and protection by CAMSAP proteins. Nat. Struct. Mol. Biol. *24*, 931–943.

Aumeier, C., Schaedel, L., Gaillard, J., et al. (2016). Self-repair promotes microtubule rescue. Nat. Cell Biol. *18*, 1054–1064.

Bálint, Š., Verdeny, V.I., Sandoval, Á.Á., et al. (2013). Correlative live-cell and superresolution microscopy reveals cargo transport dynamics at microtubule intersections. Proc. Natl Acad. Sci. USA *110*, 3375–3380.

Bergman, J.P., Bovyn, M.J., Doval, F.F., et al. (2018). Cargo navigation across 3D microtubule intersections. Proc. Natl Acad. Sci. USA *115*, 537–542.

Bouchet, B.P., and Akhmanova, A. (2017). Microtubules in 3D cell motility. J. Cell Sci. *130*, 39–50.

Brouhard, G.J., and Rice, L.M. (2018). Microtubule dynamics: an interplay of biochemistry and mechanics. Nat. Rev. Mol. Cell Biol. *19*, 451–463.

de Forges, H., Pilon, A., Cantaloube, I., et al. (2016). Localized mechanical stress promotes microtubule rescue. Curr. Biol. *26*, 3399–3406.

Dimitrov, A., Quesnoit, M., Moutel, S., et al. (2008). Detection of GTP-tubulin conformation in vivo reveals a role for GTP remnants in microtubule rescues. Science *322*, 1353–1356.

Doodhi, H., Katrukha, E.A., Kapitein, L.C., et al. (2014). Mechanical and geometrical constraints control kinesin-based microtubule guidance. Curr. Biol. *24*, 322–328.

Goodson, H.V., and Jonasson, E.M. (2018). Microtubules and microtubule-associated proteins. Cold Spring Harb. Perspect. Biol. *10*, a022608.

Gu, L., Li, Y., Zhang, S., et al. (2019). Molecular resolution imaging by repetitive optical selective exposure. Nat. Methods *16*, 1114–1118.

Gu, L., Li, Y., Zhang, S., et al. (2021). Molecular-scale axial localization by repetitive optical selective exposure. Nat. Methods *18*, 369–373.

Guo, Y.T., Li, D., Zhang, S.W., et al. (2018). Visualizing intracellular organelle and cytoskeletal interactions at nanoscale resolution on millisecond timescales. Cell *175*, 1430–1442.

Hao, H., Niu, J., Xue, B., et al. (2020). Golgi-associated microtubules are fast cargo tracks and required for persistent cell migration. EMBO Rep. *21*, e48385.

Hendershott, M.C., and Vale, R.D. (2014). Regulation of microtubule minus-end dynamics by CAMSAPs and Patronin. Proc. Natl Acad. Sci. USA *111*, 5860–5865.

Jiang, K., Faltova, L., Hua, S., et al. (2018). Structural basis of formation of the microtubule minus-end-regulating CAMSAP–Katanin complex. Structure *26*, 375–382.e4.

Jiang, K., Hua, S., Mohan, R., et al. (2014). Microtubule minus-end stabilization by polymerization-driven CAMSAP deposition. Dev. Cell *28*, 295–309.

Jiang, K., Rezabkova, L., Hua, S., et al. (2017). Microtubule minus-end regulation at spindle poles by an ASPM–katanin complex. Nat. Cell Biol. *19*, 480–492.

Jin, M., Pomp, O., Shinoda, T., et al. (2017). Katanin p80, NuMA and cytoplasmic dynein cooperate to control microtubule dynamics. Sci. Rep. *7*, 39902.

Liu, Z., Xing, D., Su, Q.P., et al. (2014). Super-resolution imaging and tracking of protein–protein interactions in sub-diffraction cellular space. Nat. Commun. *5*, 4443.

Meng, W., Mushika, Y., Ichii, T., et al. (2008). Anchorage of microtubule minus ends to adherens junctions regulates epithelial cell–cell contacts. Cell *135*, 948–959.

Roll-Mecak, A. (2013). Shining light at microtubule crossroads. Science *342*, 1180–1181.

Tanaka, N., Meng, W., Nagae, S., et al. (2012). Nezha/CAMSAP3 and CAMSAP2 cooperate in epithelial-specific organization of noncentrosomal microtubules. Proc. Natl Acad. Sci. USA *109*, 20029–20034.

Toya, M., and Takeichi, M. (2016). Organization of non-centrosomal microtubules in epithelial cells. Cell Struct. Funct. *41*, 127–135.

Vemu, A., Szczesna, E., Zehr, E.A., et al. (2018). Severing enzymes amplify microtubule arrays through lattice GTP-tubulin incorporation. Science *361*, eaau1504.

Wang, C., Liu, W., Wang, G., et al. (2017). KTN80 confers precision to microtubule severing by specific targeting of katanin complexes in plant cells. EMBO J. *36*, 3435–3447.

Wang, G., Wang, C., Liu, W., et al. (2018). Augmin antagonizes katanin at microtubule crossovers to control the dynamic organization of plant cortical arrays. Curr. Biol. *28*, 1311–1317.

Wightman, R., Chomicki, G., Kumar, M., et al. (2013). SPIRAL2 determines plant microtubule organization by modulating microtubule severing. Curr. Biol. *23*, 1902–1907.

Zhang, Q., Fishel, E., Bertroche, T., et al. (2013). Microtubule severing at crossover sites by katanin generates ordered cortical microtubule arrays in Arabidopsis. Curr. Biol. *23*, 2191–2195.

Zhou, Z., Xu, H., Li, Y., et al. (2020). CAMSAP1 breaks the homeostatic microtubule network to instruct neuronal polarity. Proc. Natl Acad. Sci. USA *117*, 22193–22203.

Received November 10, 2022. Revised March 14, 2023. Accepted August 10, 2023.